Microcavity-Enhanced Surface-Emitted Second-Harmonic Generation for Ultrafast All-Optical Signal Processing

Todd G. Ulmer, Marc Hanna, Brian R. Washburn, Stephen E. Ralph, and Anthony J. SpringThorpe

***Abstract*—By incorporating an integrated microcavity into an optical waveguide structure with vertical quasi-phase-matching, we have realized surface-emitted second-harmonic generation devices that significantly enhance the conversion efficiency for optical pulses in the picosecond and sub-picosecond regimes. We demonstrate both theoretically and experimentally that nonlinear interactions involving short optical pulses can be enhanced by a microcavity, even when the resonance width is substantially narrower than the spectral content of the pulse. The resulting enhancement enables practical signal processing functions such as ultrafast optical time-division demultiplexing at 1.55 μm in multilayer AlGaAs structures.**

***Index Terms*—Frequency conversion, integrated optics, nonlinear optics, optical resonators, optical signal processing, optical waveguides, semiconductor waveguides, ultrafast optics.**

I. Introduction

SURFACE-EMITTED second-harmonic generation (SESHG) [1] offers a unique means for ultrafast optical signal processing in a simple, integrated, nonlinear optical waveguide. Indeed, many useful device applications have been demonstrated, from integrated optical correlators [2] and spectrometers [3] to optical serial-to-parallel converters for time-division demultiplexing [4], [5]. Such novel integrated devices can serve as enabling technologies for advanced all-optical signal processing applications. For example, practical and efficient all-optical demultiplexing techniques for ultrafast optical time-division multiplexing (OTDM) have immediate applicability in high-speed optical networks.

The entire class of devices that exploit the large $\chi^{(2)}$ of III–V semiconductors may be expected to have inherent efficiency advantages over $\chi^{(3)}$-based device concepts. For example, periodically poled lithium niobate has been used with much success for a variety of applications that benefit from a collinear geometry [6]–[9]. In contrast, the surface-emitting geometry (Fig. 1) produces a second-harmonic signal with a wave vector that is orthogonal to the counter-propagating fundamental wave vectors. Thus, phase matching is required in the vertical direction, and can be readily accomplished using epitaxial growth techniques [10]. The large $\chi^{(2)}$ of III–V semiconductors allows significant conversion efficiency, even for pulsed fundamental waves and the commensurate short overlap lengths associated with the surface-emitting geometry. Therefore, devices such as correlators and spectrometers that make use of signal averaging techniques are practical. However, all-optical demultiplexers cannot utilize such techniques; therefore, enhancement of the SESHG process is needed in order for practical short-pulse devices to be realized.

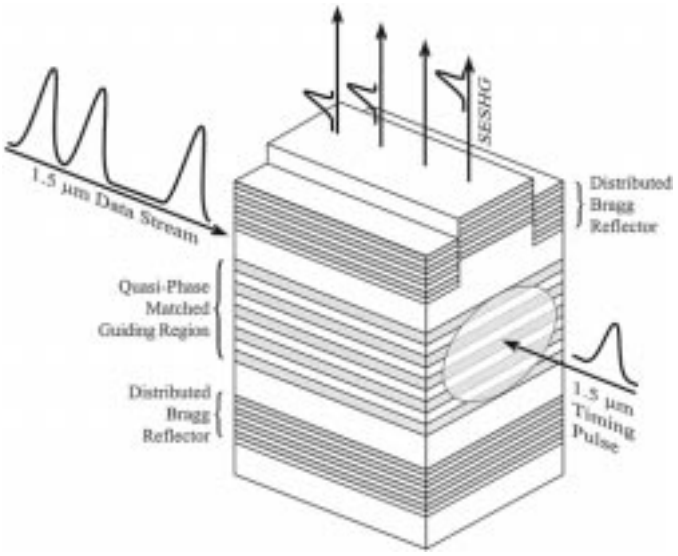

Fig. 1. Structure and operation of the SESHG device using a resonant vertical cavity integrated with a channel waveguide. All-optical demultiplexing is depicted in which a data stream comprises one fundamental wave and a counter-propagating timing pulse comprises the other fundamental wave. The upconverted data stream is emitted from the top surface.

A vertical microcavity resonant at the second-harmonic frequency can dramatically enhance the SESHG conversion efficiency. By incorporating properly positioned distributed Bragg reflectors (DBRs) both above and below the SESHG waveguide, in a geometry similar to that of a vertical-cavity surface-emitting laser (VCSEL), the majority of the second harmonic radiation is folded back upon the interacting fundamental pulses in a coherent fashion. The microcavity effectively increases the interaction length; epitaxial growth techniques allow the microcavity to be sufficiently small such that multiple round trips of

Manuscript received June 12, 2001. This work was supported by the Ultrafast Optical Communications Consortium (BellSouth, Corning, Nortel Networks, and the Georgia Research Alliance).

T. G. Ulmer was with the School of Electrical and Computer Engineering, Georgia Institute of Technology, Atlanta, GA 30332-0250 USA. He is now with the MIT Lincoln Laboratory, Lexington, MA 02420 USA.

M. Hanna, B. R. Washburn, and S. E. Ralph are with the School of Electrical and Computer Engineering, Georgia Institute of Technology, Atlanta, GA 30332-0250 USA (e-mail: stephen.ralph@ee.gatech.edu).

A. J. SpringThorpe is with Nortel Networks Optical Components Corporation, Department 5C24, Ottawa, ON K2H 8E9, Canada.

Publisher Item Identifier S 0018-9197(02)00171-9.

the second harmonic radiation occur during the overlap time of the fundamental pulses, even for sub-picosecond pulses.

The realized enhancement depends on the spectral content and temporal duration of the fundamental pulses. While enhancements of up to two orders of magnitude have been reported in the quasi-CW regime, where the bandwidth of the second harmonic is small compared to the resonance width of the cavity [11]–[14], the short-pulse regime has not been explored. For pulse widths on the order of a few picoseconds or less, the spectral content of the pulse is comparable to or larger than the cavity resonance, and the spectral filtering of the cavity must be accounted for explicitly. In the short-pulse regime, the temporal behavior of the second-harmonic pulse is also altered. Although second-harmonic photons are only generated inside the cavity during the time that the counter-propagating fundamental pulses are spatially overlapped, typical microcavities allow the average second harmonic radiation photon to make many round trips in the cavity before being transmitted through one of the high-reflectance mirrors. The second harmonic radiation power emitted from the cavity assumes an exponentially decaying temporal characteristic with a photon lifetime determined by the mirror reflectances, the mirror separation, and the cavity loss. This modified temporal response must be considered in applications such as OTDM, where intersymbol interference within the high-rate data stream must be avoided. However, it will be shown below that the optimum cavity parameters often result in cavity lifetimes of a few picoseconds or less while still providing significant enhancement. Thus, microcavity enhancement is practical for optical data streams such that the demultiplexed data rate is as high as 40 Gb/s.

Here we present a theoretical analysis of microcavity-enhanced SESHG, and show that it correctly describes the experimentally observed behavior. Furthermore, we demonstrate that significant enhancement is possible for pulses on the order of a few hundred femtoseconds, enabling new ultrafast device applications. We consider cavities with mirror separations on the order of $\sim$0.5–3 μm, corresponding to 5–30 $\lambda^{\mathrm{SH}}/2n$, and focus on AlGaAs devices designed to operate with fundamental wavelengths near 1.55 μm. We begin with a description of the efficiency calculation via the SESHG nonlinear cross-section (Section II). The total efficiency is determined from the product of the base efficiency for the waveguide structure and the enhancement factor due to the cavity. We then derive an expression for the microcavity enhancement and discuss several special cases (Section III). We also show how to optimize the cavity parameters based on the characteristics of the input pulses (Section IV). Finally, we present experimental results and show that both the spectrum and enhancement are accurately predicted, confirming the validity of the theory (Section V).

II. SESHG Efficiency Calculation

A. Overview

The geometry for SESHG is shown in Fig. 1. Counter-propagating fundamental pulses in the waveguide interact to produce a nonlinear polarization that radiates second harmonic radiation light in the vertical direction; symmetry requires that equal amounts of second harmonic radiation be radiated both up and down [15]. The figure depicts a data stream optically demultiplexed via the counter propagating timing pulse. Each collision of a data stream pulse with the timing pulse generates a surface emitted second harmonic radiation signal at a different location along the waveguide. A multilayer waveguide core is used to establish a quasi-phase-matching (QPM) condition [3], [10], allowing the second harmonic radiation field to accumulate constructively over multiple $\lambda/2n$ layers. In the absence of a microcavity, the temporal envelope of the SESHG pulse is the convolution of the fundamental pulses [16], while the spatial distribution of second harmonic radiation along the length of the waveguide is the correlation of the fundamental pulses [2]. A DBR incorporated beneath the waveguide core redirects the downward-propagating second harmonic radiation light toward the surface [17]. Since the reflected second harmonic radiation is coherent with the upward-emitted second harmonic radiation, the net efficiency is determined by the relative phase of these two second harmonic radiation components. As described in Section III, the resulting interference can either enhance or detract from the net surface-emitted second harmonic radiation.

By incorporating a second DBR above the QPM waveguide, a vertical microcavity is formed, significantly altering the performance. The total second harmonic radiation can be described by the product of a base efficiency, defined as that obtained without the resonant cavity, and a frequency-dependent enhancement factor that results solely from the cavity. The frequency variation of the linear optical index n and the nonlinear susceptibility $\chi^{(2)}$ are small, and the QPM core is broadband due to the small number of layers (typically ten or fewer); therefore, the net frequency dependence is dominated by the cavity.

B. Base Efficiency

The base efficiency is calculated using a Green's function approach [2], [18], which allows the determination of the single-pass second harmonic radiation from arbitrary nonlinear source terms. The complex amplitude of the second-harmonic electric field emitted toward the surface in the absence of a microcavity is

$$E_x^{\mathrm{SH}}(z) = \int_{-\infty}^{z} \frac{-ik_{\mathrm{o}}}{2\varepsilon(z')} P_{NL}(z') \exp\left(-i\int_{z'}^{z} k(z'')\,dz''\right) dz' \tag{1}$$

where

- z — propagation direction of the second harmonic radiation, which is coincident with the epitaxial growth direction;
- k_{o} — free-space wave number for the second harmonic radiation;
- ε — $= \varepsilon_r \varepsilon_{\mathrm{o}}$—complex permittivity;
- $P_{NL}(z)$ — spatially dependent nonlinear polarization;
- k — wavenumber in the designated material which, in general, is complex.

The second integral accounts for the phase accumulation of the wave emitted by each source term to the top of the structure. Equation (1) neglects the effects of the small reflections at the interfaces of the multilayer structures used to achieve vertical

QPM; however, these effects are small for AlGaAs waveguides. Furthermore, we have verified the accuracy of (1) by comparison to an exact transfer matrix calculation; indeed, the interface reflections cancel for vertically symmetric structures.

The SESHG interaction is dependent on both the crystal orientation and the polarization. The only nonzero elements of the second-order susceptibility tensor for $\bar{4}3m$ materials such as AlGaAs are $d_{14} = d_{25} = d_{36}$. Thus, the counter-propagating fundamental fields must be cross-polarized in standard [001]-oriented material with waveguide facets defined by the $\{110\}$ natural cleavage planes. However, it has been shown that the optimum efficiency is obtained using TE-polarized fundamental fields in [112]-oriented material [19], which maintains the important advantage of allowing the waveguide facets to be defined by cleaving. In this case, $P_{NL}^{[112]}(z) = (4/\sqrt{3})\varepsilon_o d_{14}(z) E_+^{(\omega)}(z) E_-^{(\omega)}(z)$, where $E_+^{(\omega)}$ and $E_-^{(\omega)}$ are the counter-propagating electric field strengths. Note that the SESHG efficiency is sensitive to the polarization of the fundamental pulses regardless of the material orientation.

The SESHG efficiency is often described in terms of a nonlinear cross-section A^{NL}, which relates the second-harmonic area intensity I^{SH} to the line intensities of the counter-propagating fundamentals $I_\pm^{(\omega)}$ [3], [20], [21]

$$I^{\mathrm{SH}} = A^{NL} \cdot I_+^{(\omega)} \cdot I_-^{(\omega)}. \tag{2}$$

The variation of the fundamental mode profile along the second harmonic radiation propagation direction (vertical in Fig. 1) is incorporated into the nonlinear cross-section A^{NL}. This allows for comparison of different waveguide structures. Thus, the nonlinear cross-section is defined in terms of power via

$$\frac{P^{\mathrm{SH}}}{L \cdot w^{\mathrm{SH}}} = A^{NL} \frac{P_+^{(\omega)}}{w^{(\omega)}} \frac{P_-^{(\omega)}}{w^{(\omega)}} \tag{3}$$

where

- L overlap length defined either by the length of the waveguide or, for short pulses, by the overlap length of the fundamental pulses inside the waveguide;
- w^{SH} width of the second harmonic radiation beam;
- $w^{(\omega)}$ effective width of the fundamental waveguide mode.

A^{NL} can be calculated from the nonlinear polarization $P_{NL}(z)$ and the material structure using (1). We note that some authors normalize A^{NL} to an area of 1 mm $\times$ 1 cm; however, this practice is not used here. Early nonlinear cross-section values reported for non-QPM lithium niobate waveguides were on the order of 10^{-13} W^{-1} [20], while more recent QPM AlGaAs [3] and polymer structures [21] have been reported with nonlinear cross-sections above 10^{-6} W^{-1} for a fundamental wavelength at 1.064 nm. A nonlinear cross-section of 10^{-5} W^{-1} at $\lambda = 1.55$ μm is desired for practical OTDM demultiplexing [5]; this level of performance is difficult to achieve at wavelengths far from the band-gap resonance.

C. Cavity-Enhancement Factor

The frequency-dependent cavity-enhancement factor is determined by calculating the total field outside the cavity resulting from a single plane-wave source within the cavity [22] that emits equally in both directions [15]. The net enhancement is obtained by integration over the spectral content of the second harmonic radiation pulse. The enhancement is $\Gamma = \int P_t^{\mathrm{SH}}(\omega)\, d\omega / \int P_o^{\mathrm{SH}}(\omega)\, d\omega$, where $P_t^{\mathrm{SH}}(\omega)$ is the power spectrum of the second harmonic radiation transmitted through the top of the microcavity and $P_o^{\mathrm{SH}}(\omega)$ is the power spectrum of the upward-propagating second harmonic radiation generated in the absence of a microcavity.

In the short-pulse regime, the cavity significantly modifies the temporal characteristics of the second harmonic radiation pulse. Therefore, it is useful to describe the efficiency in terms of pulse energies to facilitate comparison with experiment. The base nonlinear cross-section for Gaussian pulses is

$$A_o^{NL} = \frac{w^{(\omega)}}{\mathcal{E}_+^{(\omega)}} \frac{w^{(\omega)}}{\mathcal{E}_-^{(\omega)}} \frac{\mathcal{E}^{\mathrm{SH}}}{w^{\mathrm{SH}}} \frac{2\xi}{v_g} \tag{4}$$

where

- $\mathcal{E}^{\mathrm{SH}}$ second harmonic radiation pulse energy;
- $\mathcal{E}_\pm^{(\omega)}$ counter-propagating fundamental pulse energies;
- v_g group velocity of the fundamental;
- ξ $\sqrt{\pi/4\ln 2}$—a factor relating peak power and temporal width to energy.

Inclusion of the cavity effects yields an effective cross-section $A_{\mathrm{eff}}^{NL} = A_o^{NL}\Gamma$.

D. Numerical Implementation

A complete numerical model of microcavity SESHG has been implemented to compare the expected SESHG spectrum and efficiency to the experimental data for the structures described below. The counter-propagating fundamental pulses are described in the temporal domain by their field envelopes, and the temporal shape of the generated second harmonic radiation polarization is obtained by performing a convolution between the two fundamental fields. The second harmonic radiation polarization is then Fourier transformed, and the spatial integration described in (1) is carried out numerically for each frequency component to obtain the second harmonic radiation signal that would be produced without a cavity. This integral depends on the waveguide structure and on the vertical mode profile of the fundamental, which is obtained using a commercial software package based on a finite-difference beam-propagation method. The frequency-dependent base efficiency A_0^{NL} is then obtained from the calculated second harmonic radiation field using (3). The cavity effects are incorporated into the model by use of an iterative computation equivalent to (5), yielding the magnitude and phase of the enhanced output second harmonic radiation field in the frequency domain; the calculation incorporates the complex reflectivities of the top and bottom mirrors, which are obtained via a transfer-matrix approach. The total output power is then evaluated by integrating the second harmonic radiation power spectral density transmitted through the top mirror. Comparison with the nonenhanced second harmonic radiation power yields the total enhancement factor Γ. Since the spectral phase is included at every step of the calculation, the temporal envelope of the second harmonic radiation signal can be obtained by

applying an inverse Fourier transform to the second harmonic radiation field spectrum. The assumed d_{14} values used in the simulations are 75 pm/V for $Al_{0.25}Ga_{0.75}As$, and 18 pm/V for $Al_{0.90}Ga_{0.10}As$ [23], [24].

III. Analysis of Resonant Cavity Enhancement

A. General Resonant Cavity Enhancement Factor

Resonant cavity enhancement of SHG was first discussed by Ashkin, *et al.*, in the collinear geometry [22]. Here, we present a formulation for the surface-emitting geometry that yields the cavity enhancement as a function of frequency, inherently incorporating the spectral filtering effect of the cavity. We note that a similar approach was taken in [14]; however, here we explicitly include both the upward and downward propagating components of the second harmonic radiation, which correctly predicts the interferometric behavior described below in Section V-B. As shown in Fig. 2, the net second-harmonic field generated in the QPM core is treated as a lumped element positioned inside the cavity, allowing the enhancement factor from the cavity to be easily identified. As stated above, the net enhanced efficiency is the product of the cavity enhancement factor and the base efficiency.

The analysis is similar to that of a standard Fabry–Perot cavity, except that the field is generated inside the cavity rather than being transmitted through it. Equal-amplitude second harmonic radiation fields are generated in both the upward- and downward-propagating directions due to symmetry. The total second-harmonic field complex amplitud $E_{\text{total}}^{(2\omega)}$ at a distance l from the bottom mirror is then given by

$$\begin{aligned} E_{\text{total}}^{(2\omega)} = {} & E_{\text{o}}^{+}\left(1 + r_1 r_2 e^{-((\alpha/2)+ik)2d}\right. \\ & \left. + \left(r_1 r_2 e^{-((\alpha/2)+ik)2d}\right)^2 + \cdots\right) \\ & + E_{\text{o}}^{-} r_2 e^{-((\alpha/2)+ik)2l} \\ & \cdot \left(1 + r_1 r_2 e^{-((\alpha/2)+ik)2d}\right. \\ & \left. + \left(r_1 r_2 e^{-((\alpha/2)+ik)2d}\right)^2 + \cdots\right) \end{aligned} \tag{5}$$

where

- E_{o}^{+} upward-propagating second harmonic radiation generated in the absence of a cavity;
- r_1, r_2 complex field reflectivities of the mirrors;
- α power loss coefficient;
- d distance between the mirrors.

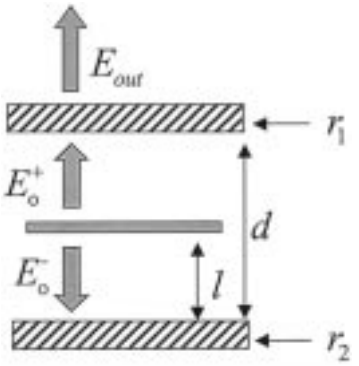

Fig. 2. Simplified cavity used to develop the general theory of resonant cavity enhancement. The mirrors are separated by a distance d, and the second-harmonic source is lumped into a single planar emitter at distance l above the lower mirror. By symmetry, equal amounts of second-harmonic light are radiated up and down.

Thus, the steady-state second-harmonic field takes the form of a pair of geometric series, and using $E_{\text{o}}^{+} = E_{\text{o}}^{+} = E_{\text{o}}$ can be written

$$E_{\text{total}} = \frac{E_{\text{o}}(1 + r_2 e^{-\alpha l} e^{-i2kl})}{1 - r_1 r_2 e^{-\alpha d} e^{-i2kd}}. \tag{6}$$

The second-harmonic field amplitude transmitted through the top mirror E_{out} is

$$E_{\text{out}} = E_{\text{total}} \cdot t_1 e^{-((\alpha/2)+ik)(d-l)} \tag{7}$$

and using $I_{\text{out}} = (1/2\eta_{\text{o}}) E_{\text{out}} E_{\text{out}}^{*}$, where η_{o} is the impedance of free space, the second harmonic radiation intensity transmitted through the top mirror is

$$\begin{aligned} I_{\text{out}} = {} & I_{\text{o}}\left(1 - |r_1|^2\right) \\ & \cdot \frac{1 + |r_2|^2 e^{-2\alpha l} + r_2 e^{-\alpha l} e^{-i2kl} + r_2^{*} e^{-\alpha l} e^{i2kl}}{1 + |r_1|^2 |r_2|^2 e^{-2\alpha d} - r_1 r_2 e^{-\alpha d} e^{-i2kd} - r_1^{*} r_2^{*} e^{-\alpha d} e^{i2kd}}. \end{aligned} \tag{8}$$

We have assumed normal incidence so that $|r|^2 + (n_t/n_c)|t|^2 = 1$, where n_c is the refractive index inside the cavity and n_t is the index of the medium above the top mirror. Furthermore, we have identified I_{o} as the upward-propagating second harmonic radiation intensity generated in the absence of the cavity

$$I_{\text{o}} = \frac{1}{2\eta_{\text{o}}} \frac{n_c}{n_t} |E_{\text{o}}^{+}|^2 e^{-\alpha(d-l)}. \tag{9}$$

Defining the complex mirror reflectivities as $r_1 = |r_1| e^{i\phi_1}$ and $r_2 = |r_2| e^{i\phi_2}$, the enhancement factor due to the resonant cavity is then found to be as in (10), shown at the bottom of the page, where P is power. The frequency dependence of the enhancement factor is contained in the wave number $k = \omega_{\text{SH}} n/c$, and also in the phase shifts from the mirrors. Reviewing the assumptions that led to (10), Γ is the power enhancement at normal in-

$$\Gamma(k) = \frac{I}{I_{\text{o}}} = \frac{P}{P_{\text{o}}} = \left(1 - |r_1|^2\right) \cdot \frac{\left(1 + |r_2| e^{-\alpha l}\right)^2 - 4|r_2| e^{-\alpha l} \sin^2\left(kl - \frac{\phi_2}{2}\right)}{\left(1 - |r_1|\,|r_2| e^{-\alpha d}\right)^2 + 4|r_1|\,|r_2| e^{-\alpha d} \sin^2\left(kd - \frac{\phi_1}{2} - \frac{\phi_2}{2}\right)} \tag{10}$$

cidence for a single plane-wave source emitting equally in both directions and positioned inside a cavity at a distance l from the bottom mirror. Microcavity-enhanced SESHG is completely described by (10) together with (1).

The form of (10) is reminiscent of the Fabry–Perot transmission function [25], although the numerator is more complicated because there are now equal and opposite second harmonic radiation field components generated inside the cavity rather than a single wave transmitted through it. Cavity resonances occur at frequencies where the single-pass phase shift in the cavity, given by $kd - (\phi_1/2) - (\phi_2/2)$, is an integral multiple of π. Constructive interference of the two second harmonic radiation components also requires positioning of the second harmonic radiation source such that $kl - (\phi_2/2)$ is an integral multiple of π. Note that for properly designed cavities, both conditions are satisfied and the standing wave peaks are centered in the core layers. High reflectivities and minimal absorption are required for large enhancements.

B. The CW Limit

For quasi-CW light, the optical bandwidth is small compared to the width of the cavity resonance. The enhancement factor given by (10) can then be taken in the single-frequency resonance limit, where the sine terms can be made exactly zero and no integration over frequency is needed. Specifically

$$\Gamma_{cw} = \left(1 - |r_1|^2\right) \cdot \frac{\left(1 + |r_2| e^{-\alpha l}\right)^2}{\left(1 - |r_1|\,|r_2| e^{-\alpha d}\right)^2}. \tag{11}$$

Implicit in (11) is the assumption that the nonlinear layers have been properly positioned inside the cavity so that constructive interference between the source and subsequent reflections is assured. In the lossless limit, there is no penalty for increasing the reflectivities as much as possible; however, this is not true for cavities with loss, as will be discussed below. As an example, assuming $\alpha = 0$ and $|r_2|^2 \approx 1$, the CW power enhancement reduces to

$$\Gamma_{CW} = \left(1 - |r_1|^2\right) \cdot \frac{4}{\left(1 - |r_1|\right)^2}. \tag{12}$$

Thus, if $R_1 = |r_1|^2 = 99\%$, the CW enhancement is $\sim$1600. This is identical to the collinear result [22], with the exception of an extra factor of four resulting from the coherent addition of the two emitted second harmonic radiation field components.

C. Enhancement From Bottom Mirror Alone

The absence of a top mirror relieves the requirement of matching the cavity resonance to the desired wavelength. This simple structure, with a reduced enhancement, may have use in less demanding applications. Using (10) with $|r_1| = 0$ in the limit where $|r_2| \to 1$ and $\alpha \to 0$, the enhancement is given by

$$\Gamma(r_1 = 0,\, r_2 = 1,\, \alpha = 0,\, \omega) = 4\cos^2\left(\frac{\omega l}{c}\, n(\omega) - \frac{\phi_2(\omega)}{2}\right). \tag{13}$$

Thus, for a specific second harmonic radiation frequency, the second harmonic radiation source may be positioned such that the reflection returns to the source with a round-trip phase shift equal to an integer multiple of 2π [e.g., when $l = p(\lambda_o/2n)$, where p is an integer, and $\phi_2 = 0$], resulting in an enhancement of four. Similarly, complete destructive interference occurs for round-trip phase shifts that are odd multiples of π. Experimental confirmation of this effect is presented in Section V. The net enhancement for a broadband pulse is not significantly reduced for most practical cases; significant reduction of the enhancement occurs only for very short pulses or large p. For the experimental microcavity structures ($p = 20$) and second harmonic radiation pulse widths characterized in this work (>100 fs), the theoretical enhancement due to the bottom mirror alone is always greater than 3.7. Similarly, we note that although the exact phase matching condition can only be maintained for a single frequency, the variation is negligible compared to the influence of the cavity.

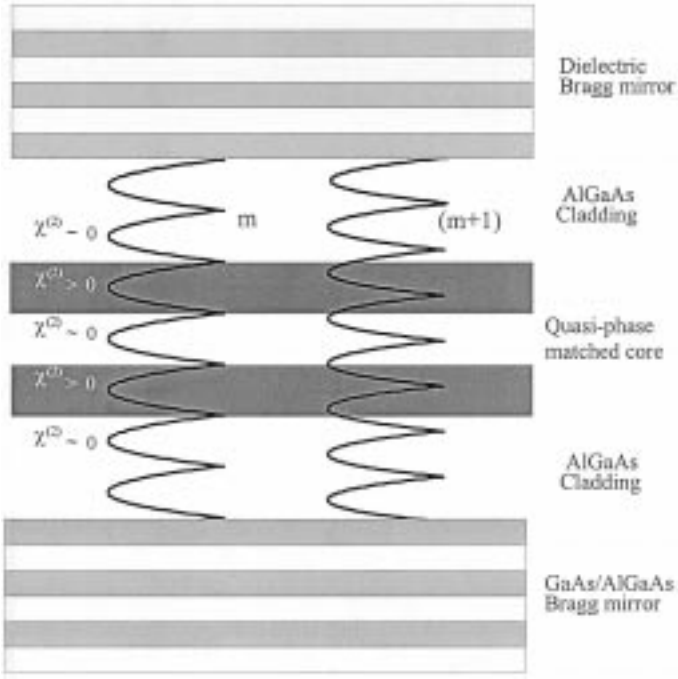

Fig. 3. Intensity distribution of adjacent longitudinal modes of the resonant cavity. Overlap with the high-$\chi^{(2)}$ layers is optimized for the mth mode; the $(m+1)$th mode has nodes at or near center of the high-$\chi^{(2)}$ layers, resulting in low second-harmonic conversion efficiency.

D. Constructive and Destructive Microcavity Resonances

The interference effects become increasingly important when the vertical cavity is completed by the addition of a top DBR. As with any optical cavity, resonances occur at frequencies where the round-trip phase shift is an integral multiple of 2π. Neglecting phase shifts at the mirrors, this condition is met when the optical path length between the mirrors corresponds to an integral number of half-wavelengths. For the microcavities considered here, the number of half wavelengths is relatively small (5–30) and care must be taken to ensure proper excitation of the cavity modes. This situation is differentiated from that encountered in larger cavities with narrow mode spacing and with uniform gain media. It is also differentiated from VCSEL cavities with narrow quantum-well gain regions, which are typically

designed with very small cavities so that they operate in a lower order mode (typically 1-λ cavities).

The standing waves associated with the cavity resonances are shown for two adjacent resonances in Fig. 3, where a resonance with m half-wavelengths is designated the mth longitudinal mode of the cavity. Note that two adjacent modes have exactly the opposite standing wave distribution at the center of the cavity, where the fundamental mode intensity is largest; specifically, if the mth mode has a peak at the center of the cavity, the $(m+1)$th mode has a node. This has a dramatic effect on the SESHG efficiency. The QPM layers in an SESHG structure are designed to be a half-wavelength thick at the second harmonic radiation wavelength and can, therefore, be positioned so that the standing wave peaks occur at the center of each of the high-$\chi^{(2)}$ layers of the QPM region. This positioning produces constructive interference between the reflected second harmonic radiation and newly generated second harmonic radiation in the core, resulting in enhanced efficiency. However, at the adjacent cavity resonances, corresponding to $m \pm 1$, the standing waves have nodes at or near the center of each of the high-$\chi^{(2)}$ layers of the QPM region, producing destructive interference of the second harmonic radiation and low net conversion efficiency. Thus, when the mth mode has a peak at the center of the cavity, the $m \pm 2$ modes have standing wave peaks approximately centered in the high-$\chi^{(2)}$ QPM layers, and a peak at the center of the cavity. Thus, constructive interference and high second harmonic radiation efficiency occur only for every other cavity resonance, and maximum efficiency occurs at the design wavelength of the QPM layers. Note that Fig. 3 depicts a QPM core with only two high $\chi^{(2)}$ layers; however, efficient structures typically incorporate more than two layers with a high $\chi^{(2)}$ layer in the center of the cavity where the fundamental intensity is highest.

The vertical microcavities considered here have dimensions of up to a few microns, resulting in adjacent cavity resonances spaced by ~20 nm for second harmonic radiation near 775 nm. The penetration into the DBRs accounts for up to 50% of the total effective cavity dimension, significantly limiting the minimum effective cavity height. The high-reflectance bandwidth of the DBRs is ~50 nm in this region by the moderate index contrast achievable in $Al_xGa_{1-x}As$ DBRs; these structures can, therefore, support up to three cavity resonances, with only every other resonance providing constructive SHG. In practice, the structure is designed for a single wavelength near the center of the DBR peak.

E. Cavity Enhancement for Short Pulses: Spectral Filtering

The frequency dependence of the cavity enhancement must be incorporated for short pulses with significant bandwidth. In this case, the total output power is obtained by integrating over ω

$$P_{\text{out}} = \int \Gamma(\omega) \cdot P_{\text{o}}(\omega)\, d\omega \tag{14}$$

where $P_{\text{o}}(\omega)$ is the power spectrum of the nonenhanced second harmonic radiation pulse. The importance of the spectral filtering effect of the cavity can be understood by noting that the second harmonic radiation spectral width for Gaussian transform-limited 1-ps, 1.55-μm fundamental pulses is 1.25 nm, which is comparable to the resonance width of a 20-$\lambda/2n$ cavity with a finesse ~30. Even with this low-finesse cavity, the spectral filtering must clearly be incorporated.

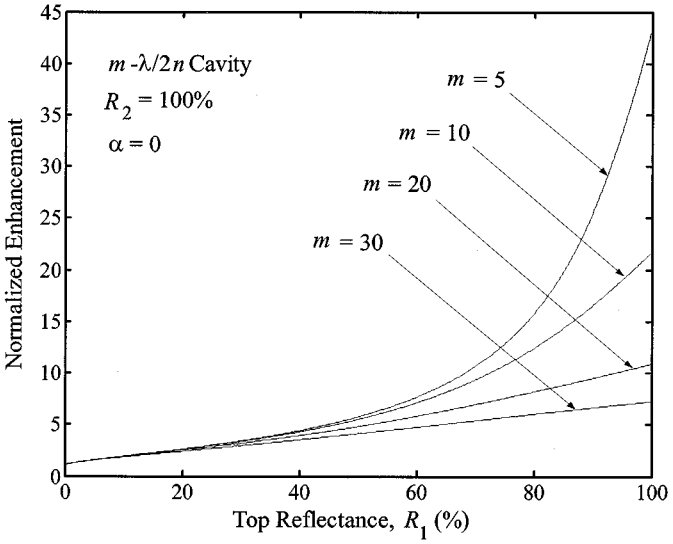

Fig. 4. Normalized enhancement for an ideal cavity with no absorption and lower mirror reflectance = 100%. Fundamental pulses are assumed to be 200-fs long and transform-limited. The enhancement increases monotonically with the top reflectance, and larger enhancements are obtained for smaller cavities.

For practical cavities ($R < 1.0$, nonzero α), the cavity parameters must be optimized for maximum second harmonic radiation efficiency. For surface-emitting devices, the bottom mirror reflectance should be the largest practically achievable value. Real losses associated with absorption and scattering inside the cavity as well as the effective loss of light transmitted through the bottom mirror result in an efficiency penalty for top reflectances beyond the optimum value. For a given cavity height and bottom reflectance, the top mirror reflectance can be optimized for a particular pulse spectrum and effective absorption.

The cavity height d plays an interesting role in this optimization. The peak enhancement at the resonant frequency increases with the finesse, which is independent of d for cavities without absorption. In contrast, the spectral width of the resonance is inversely proportional to d [26] and, therefore, a wider resonance is obtained in a smaller cavity. Thus, for a given pair of mirror reflectances (i.e., a given finesse), the spectral overlap of the resonance and the power spectrum of the nonenhanced second harmonic radiation pulse is increased in a smaller cavity, resulting in a larger net enhancement. In order to better accommodate a large pulse spectrum for short-pulse operation, it is therefore desirable to make the cavity as small as possible [27]. The benefit of smaller cavities is further quantified via numerical analysis in Section IV.

F. Ideal Cavities

Before turning to the optimization of realizable cavities, we consider the effects of various cavity and pulse parameters separately. Specifically, we examine the effects of cavity size, pulse width, and a nonideal bottom mirror. We first examine the effect of cavity size by considering the idealized case where the bottom mirror has a reflectance of 1.0 and the cavity absorption is zero. The enhancement for 200-fs fundamental pulses is

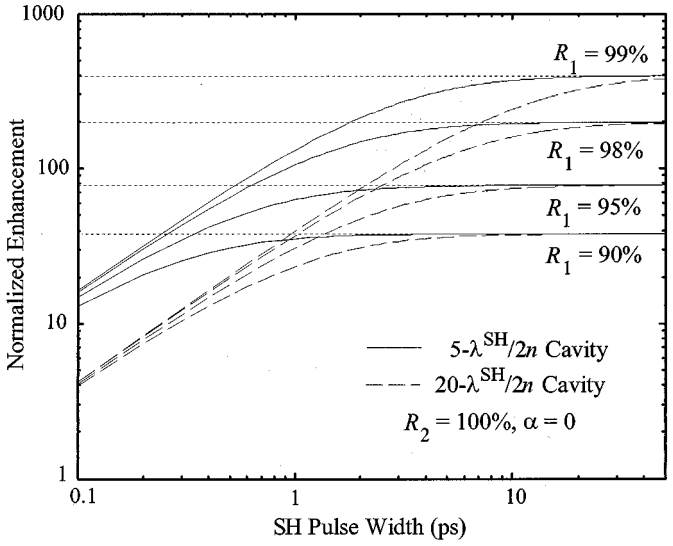

Fig. 5. Total resonant cavity enhancement as a function of transform-limited pulse width for an ideal lower mirror and no loss inside the cavity. Although the spectral width of the pulse may exceed the cavity resonance width, there is no optimum cavity finesse, i.e., increasing reflectivity always improves the enhancement. Note that for the cavity dimensions shown, the CW limit is approached for pulse widths exceeding 10 ps.

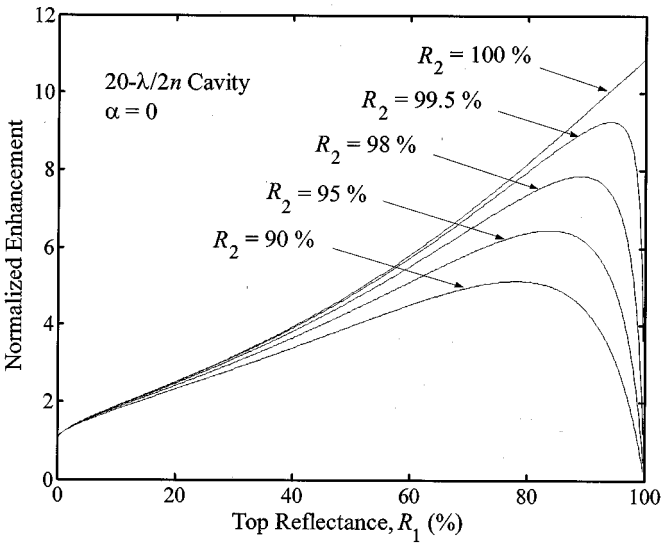

Fig. 6. Normalized enhancement for cavities with nonideal lower mirrors. Fundamental pulses are assumed to be 200-fs long and transform limited. In this case, there is an optimum cavity finesse that depends upon the cavity height and the mirror reflectances.

calculated via (14) and normalized to the case where the top reflectance is zero. The results are shown in Fig. 4 as a function of top mirror reflectance R_1 for four different cavity sizes. As described above, the enhancement factor is larger for smaller cavities. Note also that for each cavity, the enhancement factor increases monotonically with the top reflectance. In other words, as the cavity finesse is increased, the enhancement near the resonance peak increases faster than the enhancement of the spectral wings decreases. Thus, for a cavity with a perfectly reflecting bottom mirror and no absorption, there is *not* an optimum top reflectance; a larger enhancement factor is always obtained for a higher top reflectance as long as R_1 is not identically 100%.

The absence of an optimum top reflectance is also seen in Fig. 5, where the normalized cavity enhancement is shown as a function of pulse width for transform-limited Gaussian pulses. The spectral filtering effect of the cavity is apparent in the reduced enhancement for short pulses. Note that for longer pulse widths, the enhancement approaches the CW limit. Of importance is that when the bottom reflectance is unity, higher top reflectance results in a larger enhancement for all pulse widths.

In contrast, a nonideal bottom mirror acts as a source of loss in the cavity, resulting in the existence of an optimum top reflectance for a given pulse width. Thus, for any practical cavity where the bottom mirror has a reflectance of less than unity, there is an optimum value of top reflectance. The effect of a nonideal bottom mirror is shown in Fig. 6, where the normalized enhancement is again calculated via (14) assuming 200-fs Gaussian fundamental pulses. Note that the enhancement drops sharply once the optimum top reflectance is exceeded. Because the cavity absorption is assumed to be zero and the second harmonic radiation power spectrum is assumed to be constant, this sharp drop is due only to light escaping through the bottom mirror. As will be seen in Section IV, absorption and scattering losses inside the cavity produce a similar effect.

IV. Cavity Optimization for Short Pulses

In general, the enhancement of second harmonic radiation efficiency due to the resonant cavity is a function of the mirror reflectances, the absorption loss, and the spectral content of the nonenhanced second harmonic radiation pulse. To investigate the tradeoffs in practical structures, a numerical optimization of the top mirror reflectance based on (14) has been implemented. The bottom mirror is an AlGaAs DBR with a power reflectance of >99% so that most of the second harmonic radiation is emitted through the top mirror rather than into the substrate; it is optimally positioned for coherent reflection of the second harmonic radiation. The round-trip phase shift includes the penetration depth into the Bragg reflectors [28], which can be large for low-contrast mirrors. For simplicity, the refractive index and $\chi^{(2)}$ are assumed to be constant. The number of top DBR layers is then varied, and enhancement curves are calculated for several different values of cavity loss.

Results are shown in Fig. 7 for cavities with $d = 20\lambda^{\mathrm{SH}}/2n$ [Fig. 7(a) and (b)] and $d = 5\lambda^{\mathrm{SH}}/2n$ [Fig. 7(c) and (d)] for a 1.55-μm fundamental wavelength. The larger cavity has a dielectric top DBR, while the smaller cavity has an AlGaAs top DBR. Fundamental pulse widths of 1.0 ps and 200 fs are selected, resulting in nonenhanced second harmonic radiation bandwidths of 1.25 and 6.25 nm, respectively. The results are normalized to the case where $R_1 = 0$, and thus the total cavity enhancement is up to a factor of four larger than indicated.

Several trends are evident in Fig. 7. For a given cavity [i.e., comparing Fig. 7(a)–(d)], longer transform-limited pulses experience a larger enhancement, because a larger fraction of the second harmonic radiation spectrum is contained within the resonance width. The optimum top reflectance decreases slightly with decreasing pulse width, due to the increasing spectral content of the nonenhanced second harmonic radiation spectrum contained within the resonance width. The second harmonic radiation spectrum of the 1-ps pulse is peaked at the center fre-

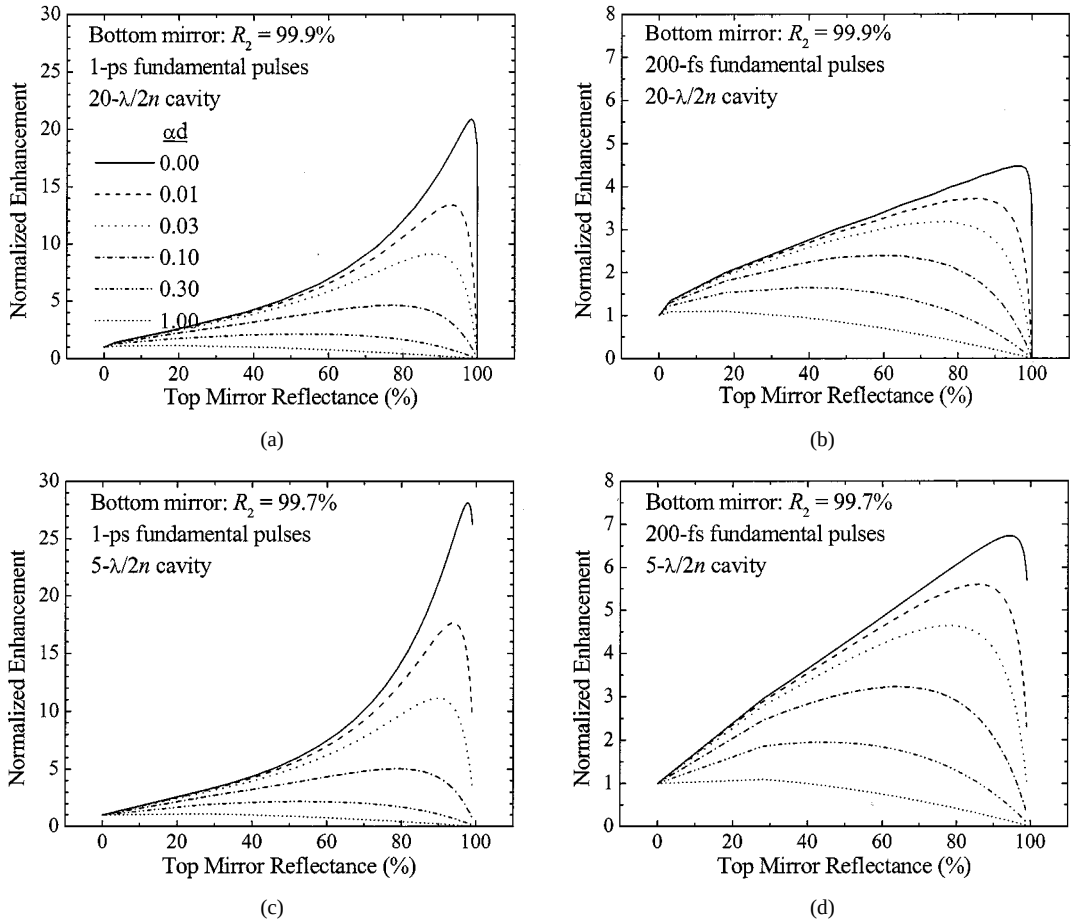

Fig. 7. Calculated resonant enhancement of second-harmonic power as a function of top mirror reflectance for two pulse widths and two cavity lengths. (a) 1-ps FWHM fundamental pulses in a 20-$\lambda/2n$ cavity. (b) 200-fs pulses in a 20-$\lambda/2n$ cavity. (c) 1-ps pulses in a 5-$\lambda/2n$ cavity. (d) 200-fs pulses in a 5-$\lambda/2n$ cavity. The cavity absorption is given by αd. All results are normalized to the case where the top mirror reflectance is zero, and thus the total enhancement is up to a factor of four larger.

quency of the resonance, while the spectrum of the 200-fs pulse is approximately constant across the width of the resonance; thus, the optimum resonance width is slightly narrower for the 1-ps pulse, corresponding to higher reflectance. With a 99.9% reflectance bottom DBR and a 20-$\lambda^{\mathrm{SH}}/2n$ cavity with no absorption, the optimum top reflectance is 98.4% for 1-ps fundamental pulses and 96.5% for 200-fs fundamental pulses, with corresponding normalized enhancements of 20.9 and 4.5, respectively.

Trends related to the cavity size and absorption are also evident in Fig. 7. As discussed in Section III-D, a larger enhancement is obtained for a smaller cavity with the same mirror reflectances, because bringing the mirrors closer together increases the spectral width of the resonance. This effect can be seen by comparing Fig. 7(a)–(c) (1-ps pulses), and Fig. 7(b)–(d) (200-fs pulses). With 1-ps fundamental pulses, the normalized enhancement is 20.9 for the 20-$\lambda^{\mathrm{SH}}/2n$ cavity and 28.7 for the 5-$\lambda^{\mathrm{SH}}/2n$ cavity; with 200-fs pulses, the corresponding enhancements are 4.5 and 6.7, respectively. The large penetration depth in the low-contrast AlGaAs DBRs presents a limitation; for the structures with AlGaAs DBRs in Fig. 7(c) and (d), the penetration depth is comparable to the mirror separation, and thus the full benefit of a smaller cavity is not realized. Clearly, structures with increased vertical confinement of the second harmonic radiation (e.g., using Al_2O_3/AlGaAs DBRs [14]) will result in even larger enhancements. Furthermore, the optimum value of top mirror reflectance decreases as the cavity absorption increases, because the second harmonic radiation experiences more loss as it makes more round trips in a higher-reflectance cavity. The cavity becomes detrimental when the absorption length is comparable to the mirror separation d, and thus minimization of absorption is critical to efficient performance. The theoretical results presented in Fig. 7(b) are compared to experimental results in Section V-C.

V. Experimental Results

A. Rear-Facet Reflection Geometry

A simple technique for measuring SESHG efficiency and spectra is shown in Fig. 8. The fundamental pulse source is an optical parametric oscillator (OPO) tunable from 1400 to 1600 nm, producing ~200-fs pulses. A single fundamental pulse is launched into the waveguide and allowed to propagate down its entire length. The Fresnel reflection R at the rear facet of the waveguide creates a counter-propagating signal, and thus SESHG is generated by the fundamental pulse reflecting back on itself. This configuration is referred to as the rear-facet

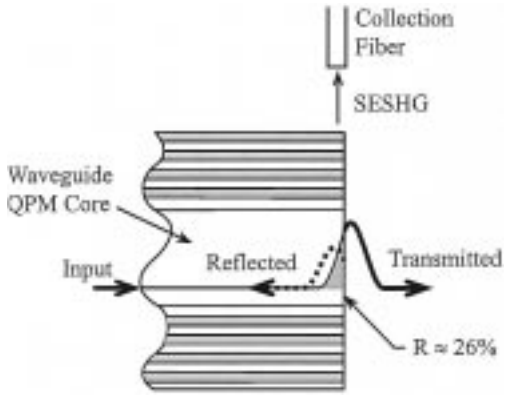

Fig. 8. Rear-facet reflection geometry for characterizing SESHG in the microcavity structure. A portion of the fundamental is reflected at the rear facet, folding the pulse back on itself, thereby creating the required collision geometry. The surface-emitted second harmonic is collected above the waveguide using an optical fiber.

reflection geometry. For efficiency measurements, the fundamental power transmitted though the waveguide is detected with an InGaAs p-i-n photodetector; measuring the transmitted power rather than the power at the waveguide input eliminates uncertainties associated with input coupling and propagation loss. The SESHG is collected with a 200-μm core optical fiber positioned above the rear facet, and detected with a silicon avalanche photodetector. The effective nonlinear cross-section can then be calculated using (4); note that $\mathcal{E}_{-}^{(\omega)} = R \cdot \mathcal{E}_{+}^{(\omega)}$ in this case, and the calculated A^{NL} must be multiplied by an additional factor of two because only half of the autocorrelation is generated in the rear-facet reflection geometry. The SESHG power spectrum is obtained using the same technique.

B. Interference

As discussed in Section III-C, the reflected downward-propagating component acquires a phase shift relative to the upward-propagating component due to the extra propagation distance and also due to the reflection at the DBR. Because the two components of the second harmonic radiation originate from the same nonlinear source, they are inherently coherent with each other. Thus, maximum SESHG is produced when the relative phase between the upward-propagating and reflected components is a multiple of 2π. Cancellation occurs when the phase shift is an odd multiple of π, with power being transferred back to the fundamental.

Experimental confirmation of this interferometric behavior is shown in Fig. 9, where the measured SESHG power as a function of input wavelength is shown for two nearly identical AlGaAs structures without top mirrors. Each structure was grown by molecular-beam epitaxy (MBE), and consists of a 4.5-period $Al_{0.25}Ga_{0.75}As/Al_{0.90}Ga_{0.10}As$ QPM waveguide core, $Al_{0.90}Ga_{0.10}As$ lower and upper cladding layers, and a 33-period $Al_{0.35}Ga_{0.65}As/AlAs$ bottom DBR designed for a reflectance of 99.9%. The key difference between the two structures is that the thickness of the cladding layers for the structure in Fig. 9(b) is specified to be larger by a factor of $\lambda/4n$ at the center DBR wavelength. Thus, the reflected downward-propagating second harmonic radiation experiences

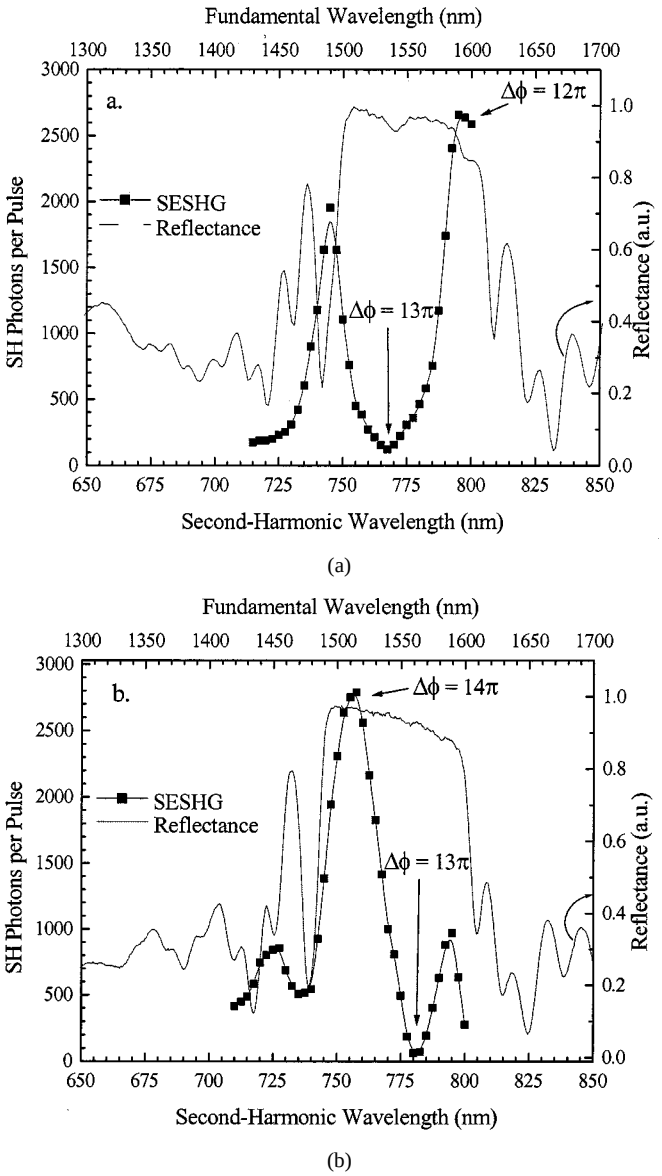

Fig. 9. Measured surface-emitted second-harmonic signal as a function of fundamental wavelength showing that every other cavity resonance is active for SESHG. The reflectance of the as-grown SESHG wafer is also shown. Interference between the upward-radiating and reflected downward-radiating components results in the strong wavelength dependence. The structure in (b) has a lower cladding layer that is a quarter-wave thicker than the structure in (a), resulting in an extra round-trip phase shift $\Delta\phi$ of π for the reflected component, shifting the wavelength dependence of the total SESHG signal.

an additional phase shift of approximately π as compared to the one in Fig. 9(a).

In Fig. 9, the second harmonic radiation signal as a function of OPO center wavelength is plotted together with the measured reflectance of the epitaxial layers. The reflectance is dominated by the broad high-reflectance peak of the DBR beneath the waveguide. The second harmonic radiation efficiency is a strong function of wavelength, as expected for an interferometric effect. Also shown for the second harmonic radiation peaks and nulls in the figure are the round-trip phase shifts from the center of the bottom high-$\chi^{(2)}$ layer to the DBR, which are determined from the design parameters. The absolute wavelengths of the corresponding peaks and nulls for the two structures do

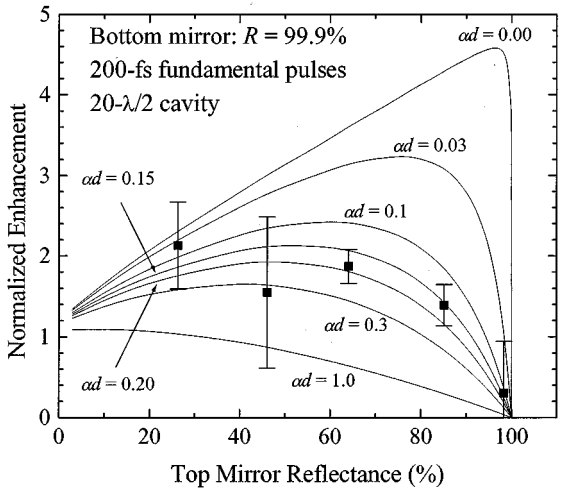

Fig. 10. Measured and predicted microcavity enhancement of SESHG efficiency for 200-fs fundamental pulses in a 20-$\lambda/2$ cavity. The estimated cavity loss is $\alpha d = 0.15$ to 0.2, corresponding to an absorption coefficient of $\alpha = 600$ cm^{-1}.

not match exactly; this is attributed to a small systematic discrepancy in the MBE growth rate. However, the expected shift of the second harmonic radiation behavior relative to the DBR center wavelength due to the extra π phase shift is observed, and the large extinction ratio confirms that the bottom DBR is highly reflective.

C. Enhancement as a Function of Reflectance

Several 20-$\lambda^{\mathrm{SH}}/2n$ microcavity structures were fabricated and characterized for comparison with the theory presented above [29], [30]. The [112] AlGaAs SESHG structure was grown by MBE, and includes a 99.9% reflectance bottom DBR, $Al_{0.90}Ga_{0.10}As$ cladding layers, and a nine-layer $Al_{0.25}Ga_{0.75}As$–$Al_{0.90}Ga_{0.10}As$ QPM core. Six samples were fabricated, each containing tens of waveguides, and a different reflectance top DBR was deposited on each sample. One sample was coated with a single quarter-wave Si_3N_4 antireflection coating ($R = 1.4\%$) to serve as the efficiency reference. Another sample was left without any dielectric coating to make use of the 26% Fresnel reflection at the top $Al_{0.90}Ga_{0.10}As$-air interface. Dielectric DBRs with 1, 2, 4, and 8 pairs of quarter-wave layers were deposited onto the four remaining samples. By comparing the measured efficiencies for the five samples with top mirrors to the AR-coated reference sample, the enhancement was obtained as a function of top mirror reflectance. Several waveguides on each sample were characterized, and the measured efficiencies averaged to arrive at the final enhancement.

The measured cavity enhancement is shown in Fig. 10 along with the theoretical predictions. As expected, the efficiency increases with the top reflectance until the loss in the cavity and the filtering of the broad pulse spectrum outweigh the enhancement at the resonance. The maximum enhancement is a factor of 2.2 relative to the AR-coated reference sample, and thus the total cavity enhancement is approximately a factor of 8.8. Exact numbers for the measured enhancement are 2.2 (normalized) and 8.8 (total). The measured enhancement indicates that the single-pass cavity loss, αd, is on the order of 0.15–0.20, corresponding to an α of 600 cm^{-1}, resulting in a single-pass transmission of $\sim$84% through the material between the mirrors. This loss may be due to both scattering and residual band-to-band absorption, and represents a critical parameter for the performance of the resonant cavity. Clearly, intracavity loss must be reduced to achieve the optimum enhancement.

As shown in Fig. 11, the performance of the microcavity is also verified by the SESHG spectra collected above the rear waveguide facet, plotted along with the corresponding numerical results. The spectral width clearly decreases as the top reflectance increases, confirming that the microcavity behaves as expected. Resonant enhancement is verified by the fact that the efficiency relative to the AR-coated sample is increased while the SESHG spectral width is reduced. In addition, the intracavity loss inferred from the observation of the spectral resonance width is in good agreement with the value obtained from the cavity enhancement ($\alpha d = 0.14$).

The measured nonlinear cross-section for the AR-coated sample is $A_0^{NL} = 1.5 \times 10^{-6}$ W^{-1}, while the theory predicts $A_0^{NL} = 5.4 \times 10^{-6}$ W^{-1}. This discrepancy may be attributed to the sensitive dependence on the fundamental power. Stray fundamental light not coupled into the waveguide mode but still collected by the photodetector reduces the A^{NL} by the square of the fundamental power. For the same structure with a four-period top DBR and negligible loss, the theoretical optimum nonlinear cross-section for 1-ps fundamental pulses is $A_0^{NL} = 2.2 \times 10^{-5}$ W^{-1}, which is more than sufficient for OTDM. Up to an additional order of magnitude improvement is potentially possible via a combination of increased confinement (reduced DBR penetration), smaller cavities [27], and domain-inverted material [31], [32].

VI. Conclusion

We have shown that the incorporation of a vertical microcavity resonant at the second harmonic radiation wavelength can greatly enhance the SESHG efficiency, even for short pulses with bandwidth that exceeds the cavity resonance width. The bottom mirror alone provides up to a factor of four enhancement; in the absence of loss, the full cavity can provide a total enhancement of $>$100 for 1-ps pulses and $>$1000 in the CW limit. For the same mirror reflectances, the resonance width is increased by decreasing the cavity size, increasing the enhancement. While the spectral filtering effect is more than compensated by the on-resonance enhancement in an ideal, lossless cavity with a perfect bottom mirror, optimization of the mirror reflectances with respect to the cavity loss and the spectral content of the pulse is required in practical structures. Loss within the cavity limits the maximum achievable enhancement, and must be minimized in order for the full benefit of the cavity to be realized.

Experimentally, we have demonstrated resonant cavity enhancement of SESHG from a 200-fs, 1.5-μm fundamental pulse using a 20-$\lambda/2n$ vertical microcavity incorporated into a quasi-phase-matched AlGaAs structure. We have also shown

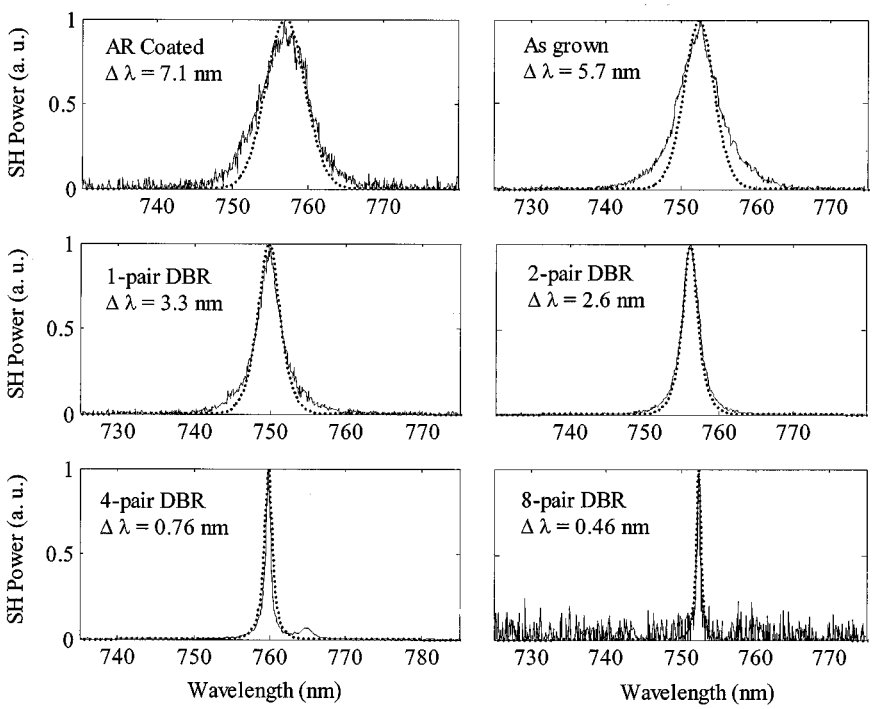

Fig. 11. Measured SESHG spectra (solid lines) plotted together with the numerically computed spectra (dotted lines) for a range of cavity finesse. The numerical computations use a fixed cavity loss ($\alpha d = 0.14$) and vary only the top mirror reflectivity. The proper scaling of the numerical and measured spectra demonstrates the validity of the theory.

that only every other cavity resonance can contribute to constructive SESHG because the nonlinear source is located within the cavity. A peak cavity enhancement of two is measured relative to an AR-coated reference sample, implying a total enhancement of eight; thus, the cavity is clearly beneficial despite the large spectral width of the pulse and the excess loss in the cavity. Significantly larger enhancements are expected in cavities with reduced loss. The maximum nonlinear cross-section for 200-fs pulses measured in this work is 3.2 $\times$ 10^{-6} W^{-1}; if material losses can be controlled, nonlinear cross-sections in excess of 10^{-5} W^{-1} should be achievable for 1-ps fundamental pulses, enabling device applications such as OTDM.

REFERENCES

[1] K. A. Shore, X. Chen, and P. Blood, "Frequency doubling and sum frequency generation in semiconductor optical waveguides," *Prog. Quant. Electr.*, vol. 20, no. 3, pp. 181–218, 1996.

[2] D. Vakhshoori and S. Wang, "Integrable semiconductor optical correlator, parametric spectrometer for communication systems," *J. Lightwave Technol.*, vol. 9, pp. 906–917, July 1991.

[3] R. Normandin, S. Létourneau, F. Chatenoud, and R. L. Williams, "Monolithic, surface-emitting, semiconductor visible lasers and spectrometers for WDM fiber communication systems," *IEEE J. Quantum Electron.*, vol. 27, pp. 1520–1530, June 1991.

[4] R. K. Tan, C. M. Verber, and A. J. SpringThorpe, "Self-timed integrated-optical serial-to-parallel converter for 100 Gbit/s time demultiplexing," *IEEE Photon. Technol. Lett.*, vol. 6, pp. 1228–1230, Oct. 1994.

[5] T. G. Ulmer, M. C. Gross, K. M. Patel, J. T. Simmons, P. W. Juodawlkis, B. R. Washburn, W. S. Astar, A. J. SpringThorpe, R. P. Kenan, C. M. Verber, and S. E. Ralph, "160-Gb/s optically time-division multiplexed link with all-optical demultiplexing," *J. Lightwave Technol.*, vol. 18, pp. 1964–1977, Dec. 2000.

[6] M. M. Fejer, G. A. Magel, D. H. Jundt, and R. L. Byer, "Quasiphase-matched second harmonic generation: Tuning and tolerances," *IEEE J. Quantum Electron.*, vol. 28, pp. 2631–2654, Nov. 1992.

[7] G. Imeshev, M. Proctor, and M. M. Fejer, "Phase correction in double-pass quasiphase-matched second-harmonic generation with a wedged crystal," *Opt. Lett.*, vol. 23, no. 3, pp. 165–167, Feb. 1, 1998.

[8] M. A. Arbore, A. Galvanauskas, D. Harter, M. H. Chou, and M. M. Fejer, "Engineerable compression of ultrashort pulses by use of second-harmonic generation in chirped-period-poled lithium niobate," *Opt. Lett.*, vol. 22, no. 17, pp. 1341–1343, Sept. 1, 1997.

[9] M. H. Chou, I. Brener, G. Lenz, R. Scotti, E. E. Chaban, J. Shmulovich, D. Philen, S. Kosinski, K. R. Parameswaren, and M. M. Fejer, "Efficient wide-band and tunable midspan spectral inverter using cascaded nonlinearities in $LiNbO_3$ waveguides," *IEEE Photon. Technol. Lett.*, vol. 12, pp. 82–84, Jan. 2000.

[10] R. Normandin, R. L. Williams, and F. Chatenoud, "Enhanced surface emitting waveguides for visible, monolithic semiconductor laser sources," *Electron. Lett.*, vol. 26, no. 25, pp. 2088–2089, Dec. 6, 1990.

[11] R. Lodenkamper, M. M. Fejer, and J. S. Harris, Jr., "Surface emitting second harmonic generation in vertical resonator," *Electron. Lett.*, vol. 27, no. 20, pp. 1882–1884, Sept. 26, 1991.

[12] R. Lodenkamper, M. L. Bortz, M. M. Fejer, K. Bacher, and J. S. Harris, Jr., "Surface-emitting second-harmonic generation in a semiconductor vertical resonator," *Opt. Lett.*, vol. 18, no. 21, pp. 1798–1800, 1993.

[13] Y. J. Ding, J. B. Khurgin, and S. J. Lee, "Cavity-enhanced and quasiphase-matched optical frequency doublers in surface-emitting geometry," *J. Opt. Soc. Amer. B*, vol. 12, no. 9, pp. 1586–1594, Sept. 1995.

[14] S. Janz, Y. Beaulieu, A. Fiore, P. Bravetti, V. Berger, E. Rosencher, and J. Nagle, "Surface emitted second-harmonic generation from a quasiphase matched waveguide in an $Al_xGa_{1-x}As/Al_2O_3$ microcavity," *Opt. Exp.*, vol. 2, no. 12, pp. 462–470, June 1998.

[15] D. Vakhshoori, "Analysis of visible surface-emitting second-harmonic generators," *J. Appl. Phys.*, vol. 70, no. 10, pp. 5205–5210, Nov. 1991.

[16] R. Normandin and G. I. Stegeman, "Picosecond signal processing with planar, nonlinear integrated optics," *Appl. Phys. Lett.*, vol. 36, no. 4, pp. 253–255, Feb. 1980.

[17] N. D. Whitbread and P. N. Robson, "Theoretical analysis of passive visible surface-emitting second-harmonic generators," *IEEE J. Quantum Electron.*, vol. 30, pp. 139–147, Jan. 1994.

[18] R. Normandin, H. Dai, S. Janz, F. Chatenoud, C. Fernando, Y. Beaulieu, and A. Delâge, "Longitudinal and vertical emission laser integration with quasi phase matched harmonic layers," *Proc. SPIE*, vol. 2139, pp. 296–308, 1994.

[19] P. A. Ramos and E. Towe, "Second-order nonlinear polarization and harmonic generation in [11*l*]-oriented III–V heterostructures," *Opt. Commun.*, vol. 132, no. 1–2, pp. 121–127, Nov. 1996.
[20] R. Normandin and G. I. Stegeman, "Nondegenerate four-wave mixing in integrated optics," *Opt. Lett.*, vol. 4, no. 2, pp. 58–59, Feb. 1979.
[21] A. Otomo, G. I. Stegeman, M. C. Flipse, M. B. J. Diemeer, W. H. G. Horsthuis, and G. R. Möhlmann, "Nonlinear contrawave mixing devices in poled-polymer waveguides," *J. Opt. Soc. Amer. B*, vol. 15, no. 2, pp. 759–772, Feb. 1998.
[22] A. Ashkin, G. D. Boyd, and J. M. Dziedzic, "Resonant optical second harmonic generation and mixing," *IEEE J. Quantum Electron.*, vol. QE-2, pp. 109–124, June 1966.
[23] I. Shoji, T. Kondo, A. Kitamoto, M. Shirane, and R. Ito, "Absolute scale of second-order nonlinear-optical coefficients," *J. Opt. Soc. Amer. B*, vol. 14, no. 9, pp. 2268–2294, Sept. 1997.
[24] R. Normandin, H. Dai, S. Janz, F. Chatenoud, C. Fernando, Y. Beaulieu, and A. Delâge, "Longitudinal and vertical emission laser integration with quasi phase matched harmonic layers," *Proc. SPIE*, vol. 2139, pp. 296–308, 1994.
[25] M. Born and E. Wolf, *Principles of Optics*, 6th ed. Cambridge, U.K.: Cambridge Univ. Press, 1980, pp. 323–333.
[26] J. T. Verdeyen, *Laser Electronics*, 3rd ed. Englewood Cliffs, NJ: Prentice-Hall, 1995, p. 151.
[27] T. G. Ulmer, M. Hanna, B. R. Washburn, C. M. Verber, S. E. Ralph, and A. J. SpringThorpe, "Microcavity-enhanced surface-emitted second-harmonic generation from 200 fs pulses at 1.5 μm," *Appl. Phys. Lett.*, vol. 78, no. 22, pp. 3406–3408, May 28, 2001.
[28] D. I. Babic and S. W. Corzine, "Analytic expressions for the reflection delay, penetration depth, and absorptance of quarter-wave dielectric mirrors," *IEEE J. Quantum Electron.*, vol. 28, pp. 514–524, Feb. 1992.
[29] T. G. Ulmer, B. R. Washburn, C. M. Verber, S. E. Ralph, and A. J. SpringThorpe, "Resonant-cavity-enhanced surface-emitted second-harmonic generation optimized for short pulses," *Proc. Ultrafast Electronics and Optoelectronics Conf.*, pp. 42–44, 2001.
[30] T. G. Ulmer, B. R. Washburn, A. J. SpringThorpe, C. M. Verber, and S. E. Ralph, "Microcavity-cavity-enhanced surface-emitted second-harmonic generation for signal processing in the ps and fs regimes," in *Ultrafast Phenomena XII*, T. Elsaesser, Ed. New York: Springer, 2000, pp. 189–191.
[31] S. Koh, T. Kondo, T. Ishiwada, C. Iwamoto, H. Ichinose, H. Yaguchi, T. Usami, Y. Shiraki, and R. Ito, "Sublattice reversal in GaAs/Si/GaAs (100) heterostructures by molecular beam epitaxy," *Jpn. J. Appl. Phys.*, pt. 2, vol. 37, no. 12B, pp. L1493–L1496, Dec. 15, 1998.
[32] C. B. Ebert, L. A. Eyres, M. M. Fejer, and J. S. Harris, Jr., "MBE growth of antiphase GaAs films using GaAs/Ge/GaAs heteroepitaxy," *J. Cryst. Growth*, vol. 210/202, pp. 187–193, 1999.

Todd G. Ulmer was born in 1970. He received the B.S. degree in physics (*magna cum laude*) from Furman University, Greenville, SC, in 1993, the B.E.E. degree (with highest honors) in 1994, and the M.S. and Ph.D. degrees in electrical engineering in 1996 and 2000, all from Georgia Institute of Technology (Georgia Tech), Atlanta.

From 1993 to 2000, he was a member of the Ultrafast Optical Communications group, Georgia Tech's Microelectronics Research Center. His dissertation research involved an integrated-optical serial-to-parallel converter for optical time-division demultiplexing that utilizes microcavity-enhanced surface-emitted second-harmonic generation in semiconductor waveguides. In 2001, he joined the Optical Communications Technology Group at Massachussetts Institute of Technology's (MIT) Lincoln Laboratory, Cambridge, MA, where he is presently investigating wide-band analog optical links, fiber Bragg gratings, and polarization controllers. His research interests also include optical time-division multiplexing, nonlinear optics in semiconductors and optical fiber, integrated optical devices, and optical switching.

Dr. Ulmer was the recipient of a Schlumberger Foundation Fellowship and a 2000 SAIC Student Paper Award. He is a member of Phi Beta Kappa, Eta Kappa Nu, Tau Beta Pi, the IEEE Lasers and Electro-Optics Society, and the Optical Society of America.

Marc Hanna was born in 1974. He received the engineering degree from the Institut National des Telecommunications, Evry, France, in 1996, and the Ph.D. degree in electrical engineering from the Universite de Franche Comte, Besancon, France, in 2000.

He is currently with the GTL-CNRS Telecom laboratory, Metz, France. His research interests include optical solitons, ultrafast optics, and optical telecommunication systems.

Brian R. Washburn was born in Racine, WI, in 1972. He received the B.S. degree (*summa cum laude*) from the University of Wisconsin-Parkside in 1994. He is currently working toward the Ph.D. degree in physics at the Georgia Institute of Technology (Georgia Tech), Atlanta, with his thesis research focusing on supercontinuum generation in microstructure fiber.

In 1995, he held a research position at Argonne National Laboratory, working on high-temperature superconductors. His current research interests include ultrafast semiconductor spectroscopy, nonlinear fiber optics, microstructure fibers and ultrashort pulse characterization.

Mr. Washburn is a member of the Optical Society of America and the IEEE Lasers and Electro-Optics (LEOS) Society.

Stephen E. Ralph received the B.E.E. degree in electrical engineering degree (with highest honors) from Georgia Institute of Technology (Georgia Tech), Atlanta, in 1980, and the Ph.D. degree in electrical engineering from Cornell University, Ithaca, NY, in 1998. His research focused on the optical detection of highly nonequilibrium transport in heterojunction devices.

In 1988, he began a postdoctoral position at AT&T Bell Laboratories. In 1990, he joined the IBM T. J. Watson Research Center, Yorktown Heights, NY. In 1992, he joined the faculty in the Physics Department, Emory University, Atlanta, GA. In 1998, he became an Associate Professor of Electrical and Computer Engineering at Georgia Tech, where his work currently focuses on the development of ultrafast optical devices for telecommunications.

Dr. Ralph is a member of the American Physical Society, the IEEE Lasers and Elecro-Optics Society, and the Optical Society of America.

Anthony J. SpringThorpe, photograph and biography not available at the time of publication.